NANO LETTERS

LETTER

pubs.acs.org/NanoLett

Graphene-Based Bimorph Microactuators

Shou-En Zhu,[†,‡] Roxana Shabani,[∥] Jonghyun Rho,[†,‡] Youngsoo Kim,[†,§] Byung Hee Hong,[†,§] Jong-Hyun Ahn,[*,†,‡] and Hyoung J. Cho[*,‡,∥]

[†]SKKU Advanced Institute of Nanotechnology (SAINT) and Center for Human Interface Nano Technology (HINT), [‡]School of Advanced Materials Science and Engineering, and [§]Department of Chemistry, Sungkyunkwan University, Suwon 440-746, Republic of Korea

[∥]Department of Mechanical, Materials and Aerospace Engineering, University of Central Florida, Orlando, Florida 32816-2450, United States

Supporting Information

ABSTRACT: A novel graphene-on-organic film fabrication method that is compatible with a batch microfabrication process was developed and used for electromechanically driven microactuators. A very thin layer of graphene sheets was monolithically integrated and the unique material characteristics of graphene including negative thermal expansion and high electrical conductivity were exploited to produce a bimorph actuation. A large displacement with rapid response was observed while maintaining the low power consumption. This enabled the successful demonstration of transparent graphene-based organic microactuators.

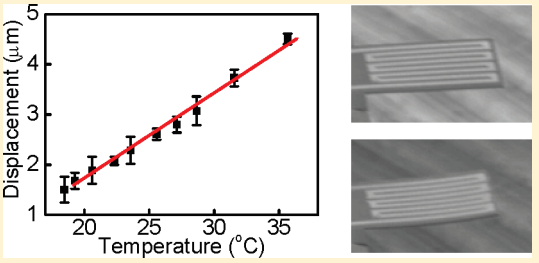

KEYWORDS: Graphene, actuator, organic, thermal, mechanical, sensor

Graphene, the thinnest elastic material, has superb electronic and mechanical properties that make it a promising host for various device applications.[1−5] In particular, graphene has a distinctive negative coefficient of thermal expansion (CTE) (contraction upon heating),[4,6] which is in contrast with the normal behavior of conventional materials. Therefore, in a case where a thin layer of graphene coupled to a different material member is heated, the asymmetric thermomechanical response may lead to large bimorph actuation.

Microactuators, which can convert electric energy directly to mechanical energy, have attracted attention for a range of biomimetic applications, including insect-like motion, flying robots, and fishlike manipulators.[7−11] These microactuators were designed to reproduce the important features of natural muscle, such as response speed, displacement, and controllability. A range of inorganic materials including shape memory alloys and piezoelectric ceramics have been evaluated as actuators.[12,13] However, the high operating temperature and voltage restrict their range of applications. On the other hand, polymer-based soft actuators including dielectric elastomers, conjugated polymers, and polymer gels have advantages, such as flexibility, lightweight, and optical transparency.[10,14,15] Nevertheless, the slow response, short life cycle, and low-energy conversion efficiency limit the performance of polymer-based actuators. More importantly, there are difficulties in their fabrication method. The majority of the listed materials require postprocessing steps or assembly methods that are not compatible with conventional batch microfabrication steps. Hence, there are significant challenges in developing actuator materials for a large displacement and a rapid response at low voltages, as well as in developing a compatible fabrication method.

Figure 1 shows a schematic diagram of the fabrication process for a graphene/epoxy hybrid bimorph actuator. First, graphene films were grown on a 4 in. SiO_2/Si wafer coated with Ni catalyst layer using the procedures described elsewhere.[16,17] The transmittance of the graphene films was ∼78.8% at the 550 nm wavelength, which indicates that the average number of graphene layers is nine because the transmittance of an individual graphene layer is reduced by ∼2.3% (Supplementary Figure S1a, Supporting Information).[18,19] The sheet resistance of graphene films was ∼200 Ω/sq measured using a four-probe Van der Pauw setup. In addition, the Raman spectra measured for graphene films on SiO_2 substrates showed a strongly suppressed defect-related D-band peak (Supplementary Figure S1b, Supporting Information). The graphene-grown wafer was cut to a 2.5 × 2.5 cm^2 piece as a handling substrate. Gold contact pads and alignment markers were fabricated by photolithography. A serpentine microheater pattern of the graphene on Ni film was formed again by photolithography and O_2 plasma reactive ion etching (RIE). Finally, a thin epoxy (SU-8) cantilever (L:W:H = 180 × 200 × 3.4 μm) with a transmittance of approximately 99% at 550 nm (Supplementary Figure S1a, Supporting Information) and a thick support body (50 μm measured by surface profilometer) were fabricated by two sequential photolithography steps.[20,21] The graphene/epoxy hybrid cantilever microactuators

Received: October 14, 2010
Revised: January 9, 2011
Published: January 31, 2011

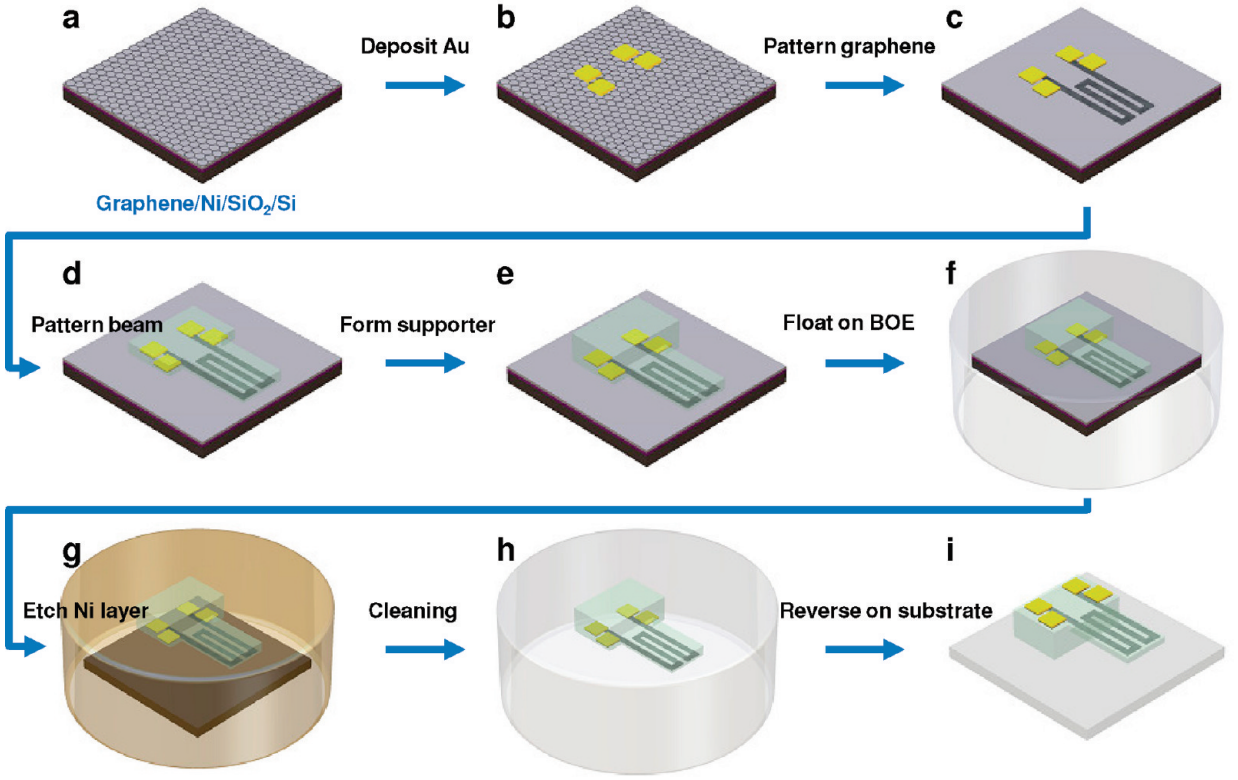

Figure 1. Schematic diagram of the fabrication process for graphene and epoxy hybrid cantilever system. (a) The process begins with the CVD synthesis of centimeter-scale graphene films on a Ni(300 nm)/SiO_2(300 nm)/Si substrate. (b) A 30 nm gold layer was deposited on graphene by thermal evaporation to define the four electrodes. (c) Conventional photolithography and RIE with O_2 plasma were employed to pattern the graphene serpentine microheater. (d, e) Two steps of epoxy photolithography were employed to form the cantilever beam and support body. (f−h) BOE and $FeCl_3$ were used to remove the nickel and SiO_2 sacrificial layers followed by rinsing in DI water to clean the cantilever. (i) The cantilever was reversed and attached on a glass support for measurement.

were transferred from the wafer substrate using a bi-sacrificial-layer wet release process. First, a buffered oxide etchant (BOE) was used to remove the SiO_2 layer (see also Figure 2a). The separated epoxy/graphene/Au/Ni layers were then transferred and soaked in an aqueous iron(III) chloride ($FeCl_3$) solution (1 M) for 5 min to remove the Ni metal layers. After the Ni dissolution, the samples were set free in the solution (see also Figure 2b). This process generates a patterned stand-alone graphene-on-organic film structure that is detached from the carrier substrate without compromising the integrity of the graphene sheets. The resulting cantilever chips were cleaned with deionized (DI) water and made ready for the test. A rigid substrate (glass, quartz or silicon wafer) was used as a support during the measurement. The resistance of the graphene ranged from 50 to 60 kΩ. This process resulted in transfer yields approaching 99%.

Figure 2c shows a field emission scanning electron microscopy (FE-SEM) image of the four arrays of the graphene−epoxy hybrid microcantilevers. The inset micrograph clarifies the typical structure of a graphene serpentine pattern and a 3.4 μm thick cantilever beam at the oblique view. The conducting graphene films were directly heated, and the organic epoxy film was warmed up by the diffused heat upon applying the electric power. The compatibility of aromatic ring structure of graphene and epoxy is believed to provide a firm $\pi-\pi$ interaction interface between these two layers, which can lead to an efficient bonding through the interface without delamination up to 0.4% strain.[5] The asymmetrical thermal expansion between the graphene and epoxy films is expected to cause upward deflection of the actuator upon heating the setup (Figure 2d).

A model of the graphene actuator was created using the simulation package (ANSYS, Inc.) where the fixed support boundary condition was applied to the base of the epoxy beam. The free convection condition was applied to all surfaces in contact with air (including the top part of the graphene layer). The uniform internal heat generation in the graphene layer was derived from electrical power divided by the graphene volume. The mechanical and thermal properties that were used as constant values are listed in Table 1.

The maximum temperature (T_{max}) of the beam is a function of the convection heat transfer coefficient (h) and electrical power (P); therefore the simulation was done by systematically changing the values of h and P. Summarizing the simulation results, a simple equation for T_{max} (°C) as a function of P (W) and h (W/m^2·°C) was obtained

$$T_{max}(h, P) = (Ah + B)P + C \quad (1)$$

where A, B, and C are -14 °C^2·m^2/W^2, 29.3×10^3 °C/mW, and 17.3 °C, respectively. Equation 1 was implemented to fit the experimental data T_{max} (P) by a chi-square minimization method following the Levenberg−Marquardt (L-M) algorithm (Figure 3a).[22,23] The only fitting parameter was h, calculated to be 1027 ± 23 (W/m^2·°C).

In the next step the beam tip deflection (d) was investigated which is a function of CTE and T_{max}. Since the deflection

dx.doi.org/10.1021/nl103618e |*Nano Lett.* 2011, 11, 977–981

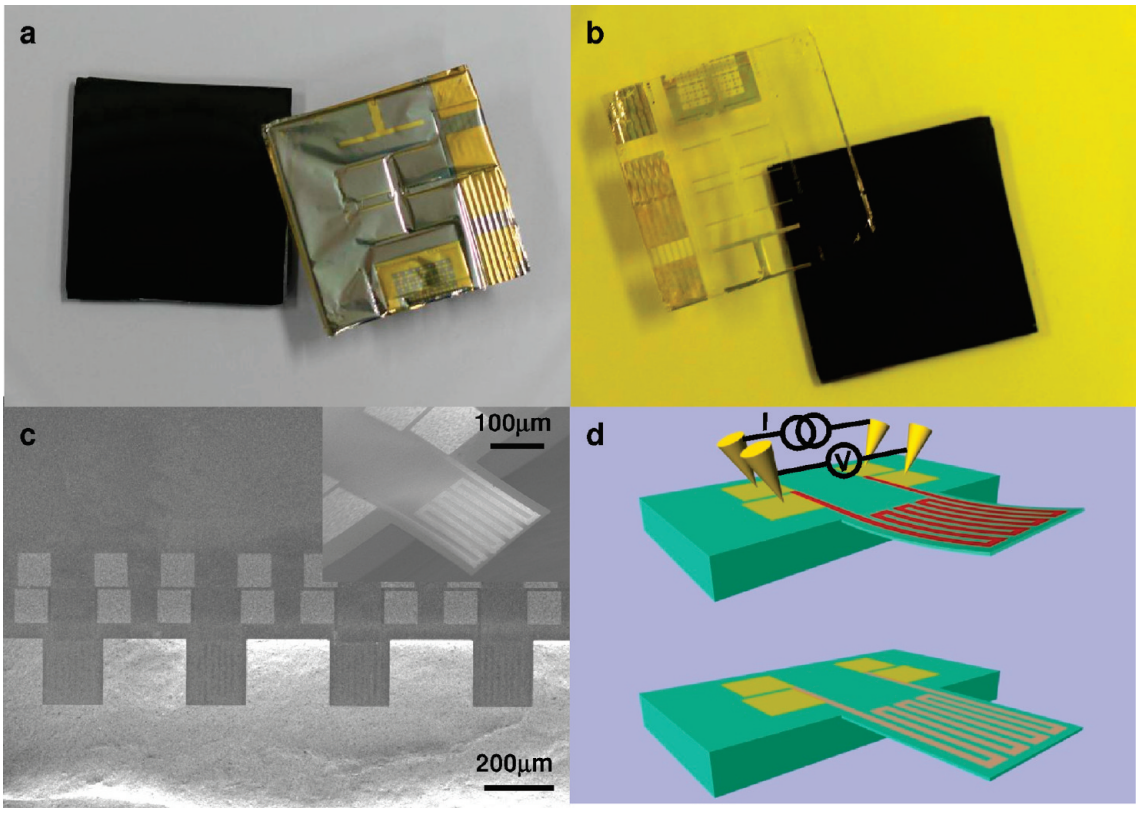

Figure 2. Optical and FE-SEM image of the hybrid cantilever beam. (a, b) A 2.5 × 2.5 cm^2 floating sample after etching the SiO_2 and nickel layers in BOE and $FeCl_3$ aqueous solution, respectively. The Si substrate was used directly as a transfer support. (c) FE-SEM (acceleration voltage = 1 kV) micrograph of the four array graphene and epoxy hybrid microcantilever. The inset micrograph clarifies the typical structure geometry of the graphene serpentine pattern and 3.4 μm epoxy cantilever beam at the oblique view. (d) Schematic diagram of the measurement setup, bottom image shows the initial stage of cantilever beam, top image shows the upward deflection upon applying the electrical power.

Table 1. Mechanical and Thermal Properties for Epoxy and Graphene Used in ANSYS Simulation

	epoxy	graphene
Young's modulus (GPa)	2	660
Poisson's ratio	0.22	0.2
density (g/cm^3)	1.233	1
thermal expansion (1/K)	5.2×10^{-5}	
thermal conductivity (W/mK)	0.3	600

measurement is independent of previous set of data, it could also be used to extract useful information about the system. Following the same procedure as in the previous part, a series of simulations were done for d (μm) at different T_{max} and CTE (/°C). The equation below was obtained for d as a function of CTE and T_{max}

$$d(\mathrm{CTE}, T_{max}) = (L \cdot \mathrm{CTE} + M)(T_{max} + N) \qquad (2)$$

where L, M, and N are -3.1×10^3 μm, 0.15 μm/°C, and −10.5 °C, respectively. Here the graphene CTE was used as the fitting parameter to fit the above equation to the measured data (Figure 3b) using the same method as the previous step, and CTE was found to be $(-6.9 \pm 0.6) \times 10^{-6}$ (/°C). This is in good agreement with the reported values.[4,6] The small error bars obtained for h and CTE demonstrate the accuracy of the values obtained for the fitting parameters. The overall layout of the beam and the graphene layer, the steady state temperature distribution of the beam from a top view, the beam deflection from a side view, the equivalent (von-Mises) elastic strain and the thermal strain of the entire beam are shown for the maximum input power in supplementary Figure S2 in the Supporting Information. The deflection is not to scale and is exaggerated for clarity. The model was clipped in two directions to show the thermal and von-Mises strain contours inside the model.

Figure 3a shows the maximum temperature of the microcantilever as a function of the input power for the measured data and the simulation results. The cantilever was actuated by increasing the temperature. At the reference temperature (~17 °C), the beam was bent down slightly (~1.5 μm), which is in agreement with the resistance (supplementary Figure S3, Supporting Information). With the onset of power input (0.02 mW), the beam rapidly bent up and became flat. As the temperature was increased, the cantilever beam bent up smoothly in the positive direction. The temperature of the cantilever changed linearly to 36 °C with a supplied power up to 1.26 mW. The deflection of the cantilever increased linearly with temperature or the electrical input power. From these plots, the effective conversion factors of 0.17 μm/°C and 2.58 μm/mW were calculated, which matches the theoretical quantitative analysis shown in Figure 3b. These conversion factors can be increased using a thinner epoxy layer. The nonsmooth transition through the zero point is an indication of the presence of initial strain in the material at rest. This can be the result of the fabrication process and the induced changes in graphene topology on the given substrate, which is consistent

dx.doi.org/10.1021/nl103618e |*Nano Lett.* 2011, 11, 977–981

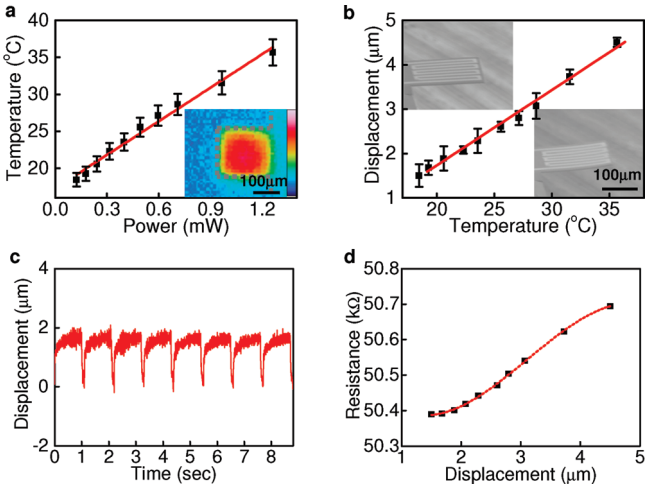

Figure 3. Performance characterization of a graphene-based organic bimorph microactuator. (a) Temperature extracted from the emitted IR radiation as a function of the input power, and the solid line shows the best fit to the data obtained by finite element analysis (FEA); the inset shows a color contour plot of the temperature profile of the cantilever, and the dotted gray lines represent the beam boundaries. Color scale from 17 to 40 °C is shown on the right. (b) Tip displacement of the cantilever beam as a function of temperature. Each data point is the average value of five measurements, and the standard deviation is shown as error bars. The solid line shows the fit to the data obtained from FEA. The insets show the SEM images of the initial position of the cantilever beam (top left) and bend up state upon applying electrical power (right bottom). (c) Tip displacement of the cantilever beam as a function of time extracted from eight repeated cycles of input sweep voltage from 1 to 4 V for 1 s followed by off power period for 0.1 s in each cycle. (d) Resistance of graphene serpentine microheater as a function of the displacement of cantilever tip. The dashed line shows a polynomial fit (order of three) to the data.

with the sudden uptake observed at the extremely low input power, as shown in Figure 3c. The tip displacement of the cantilever beam as a function of time was measured for eight repeated cycles of an input sweep voltage from 1 to 4 V for 1 s with a switching-off duration of 0.1 s. This showed the oscillation of the cantilever with a frequency of 0.91 Hz. Interestingly, this cantilever produced a very rapid response, even at a low input voltage. For an initial input of 1 V, the cantilever tip moved up to 1 μm in 0.02 s ($\sim$50 μm/s) and returned as fast as $\sim$0.1 s to its starting position ($\sim$13.3 μm/s). This might be originating from the high thermal conductivity of graphene.[24] Finally, the resistance as a function of displacement was plotted in Figure 3d. The resistance of graphene was increased due to the contribution of strain and heating during actuation. This also suggests that the graphene component can be used both for actuation and sensing, which will facilitate an optimized control. When the strain was removed, the resistance returned to its initial value, indicating that deflection is reversible in an elastic structural regime.

The reversible mechanical actuation provides a basis for the design of various organic devices. In particular, the transparency of graphene is useful for applications that require optically transparent devices. Figure 4 shows the structure of the graphene-based microactuator which has a similar form to a transparent dragonfly wing. The graphene is used for both actuation and structural support. The graphene-on-organic film actuator generates a flapping and bending movement that could be controlled by changing the frequency and the duration of the applied voltage

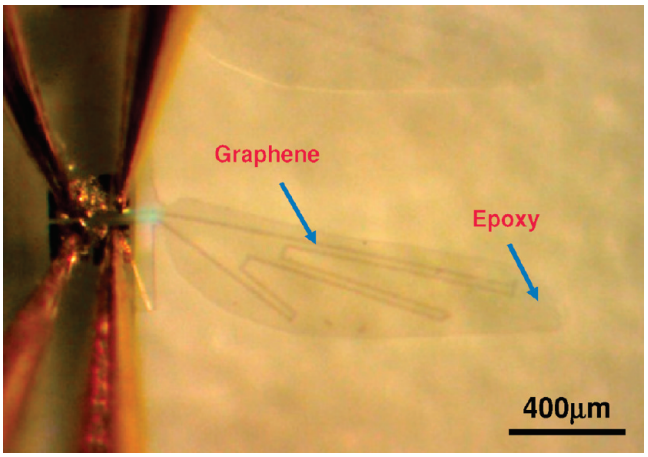

Figure 4. Graphene-on-organic film which is in the form of a dragonfly wing.

(supplementary video 1, Supporting Information). The flexibility, transparency, low weight, and patternability of the graphene based actuator system highlight its potential for many applications including biomimetic actuators, membranes, and skins.

In summary, a microactuator was developed based on a graphene-on-organic film hybrid bimorph. A new fabrication method allowed for the monolithic integration of a graphene layer as an active component. A phtolithographically defined graphene sheet resistor could be used for both actuation and sensing. The extraordinary mechanical, optical, and electrical properties of graphene were implemented into a working device.

■ ASSOCIATED CONTENT

Ⓢ Supporting Information. Characterization of the sample, simulation data, and a movie file that shows actuation. These materials are available free of charge via the Internet at http://pubs.acs.org.

■ AUTHOR INFORMATION

Corresponding Author

*E-mail: joecho@mail.ucf.edu and ahnj@skku.edu.

■ ACKNOWLEDGMENT

This was supported by Basic Science Research Program (2010-0015035), WCU Program (R32-2008-000-10124-0), and the 21st Century Frontier Research Programs (2010K-000196) through the National Research Foundation under the Ministry of Education, Science and Technology, Korea, and by the Nanotechnology Undergraduate Education Program (EEC-0741508), National Science Foundation, USA. We thank Dr. W. H. Kim at Korea Electronics Technology Institute (KETI) and Dr. W. J. Lee at Samsung electromechanics for technical assistance with strain and IR image measurements.

■ REFERENCES

(1) Novoselov, K. S.; Geim, A. K.; Morozov, S. V.; Jiang, D.; Zhang, Y.; Dubonos, S. V.; Grigorieva, I. V.; Firsov, A. A. *Science* **2004**, *306*, 666–669.
(2) Geim, A. K.; Novoselov, K. S. *Nat. Mater.* **2007**, *6*, 183–191.
(3) Lee, C.; Wei, X.; Kysar, J. W.; Hone, J. *Science* **2008**, *321*, 385–388.

(4) Bao, W.; Miao, F.; Chen, Z.; Zhang, H.; Jang, W.; Dames, C.; Lau, C. N. *Nat. Nanotechnol.* **2009**, *4*, 562–566.
(5) Gong, L.; Kinloch, I. A.; Young, R. J.; Riaz, I.; Jalil, R.; Novoselov, K. S. *Adv. Mater.* **2010**, *22*, 2694–2697.
(6) Chen, C.; Rosenblatt, S.; Bolotin, K. I.; Kalb, W.; Kim, P.; Kymissis, I.; Stormer, H. L.; Heinz, T. F.; Hone, J. *Nat. Nanotechnol.* **2009**, *4*, 861–867.
(7) Ashley, S. *Sci. Am.* **2003**, *289*, 52–59.
(8) Gu, G.; Schmid, M.; Chiu, P.-W.; Minett, A.; Fraysse, J.; Kim, G.-T.; Roth, S.; Kozlov, M.; Muñoz, E.; Baughman, R. H. *Nat. Mater.* **2003**, *2*, 316–319.
(9) Erdem, E. Y.; Chen, Y.-M.; Mohebbi, M.; Suh, J. W.; Kovacs, G.; Darling, R. B.; Böhringer, K. F. *J. Microelectromech. Syst.* **2010**, *19*, 433–442.
(10) Maeda, S.; Hara, Y.; Sakai, T.; Yoshida, R.; Hashimoto, S. *Adv. Mater.* **2007**, *19*, 3480–3484.
(11) Higuchi, T. *J. Mech. Sci. Technol.* **2010**, *24*, 13–18.
(12) Kim, B.; Lee, S.; Park, J. H.; Park, J. O. *IEEE/ASME Trans. Mechatronics* **2005**, *10*, 77–86.
(13) Lima, C. R. D.; Vatanabe, S. L.; Choi, A.; Nakasone, P. H.; Pires, R. F.; Silva, E. C. R. *Sens. Actuators, A* **2009**, *152*, 110–118.
(14) Paquette, J. W.; Kim, K. J. *IEEE J. Oceanic Eng.* **2004**, *29*, 729–737.
(15) Baughman, R. H. *Synth. Met.* **1996**, *78*, 339–353.
(16) Lee, Y.; Bae, S.; Jang, H.; Jang, S.; Zhu, S.-E.; Sim, S. H.; Song, Y. I.; Hong, B. H.; Ahn, J.-H. *Nano Lett.* **2010**, *10*, 490–493.
(17) Kim, K. S.; Zhao, Y.; Jang, H.; Lee, S. Y.; Kim, J. M.; Kim, K. S.; Ahn, J.-H.; Kim, P.; Choi, J.-Y.; Hong, B. H. *Nature* **2009**, *457*, 706–710.
(18) Nair, R. R.; Blake, P.; Grigorenko, A. N.; Novoselov, K. S.; Booth, T. J.; Stauber, T.; Peres, N. M. R.; Geim, A. K. *Science* **2008**, *320*, 1308–1308.
(19) Bae, S.; Kim, H.; Lee, Y.; Xu, X.; Park, J.-S.; Zheng, Y.; Balakrishnan, J.; Lei, T.; Kim, H. R.; Song, Y. I.; Kim, Y.-J.; Kim, K. S.; Özyilmaz, B.; Ahn, J.-H.; Hong, B. H.; Iijima, S. *Nat. Nanotechnol.* **2010**, *5*, 574–578.
(20) Nordström, M.; Keller, S.; Lillemose, M.; Johansson, A.; Dohn, S.; Haefliger, D.; Blagoi, G.; Jakobsen, M. H.; Boisen, A. *Sensors* **2008**, *8*, 1595–1612.
(21) Keller, S.; Haefliger, D.; Boisen, A. *J. Micromech. Microeng.* **2010**, *20*, 045024.
(22) Levenberg, K. *Q. Appl. Math.* **1944**, *2*, 164–168.
(23) Marquardt, D. *SIAM J. Appl. Math.* **1963**, *11*, 431–441.
(24) Seol, J. H.; Jo, I.; Moore, A. L.; Lindsay, L.; Aitken, Z. H.; Pettes, M. T.; Li, X. S.; Yao, Z.; Huang, R.; Broido, D.; Mingo, N.; Ruoff, R. S.; Shi, L. *Science* **2010**, *328*, 213–216.